Multidimensional segmentation of coronary intravascular ultrasound images using knowledge-based methods

Mark E. Olszewski,[a] Andreas Wahle,[a] Sarah C. Vigmostad,[b] and Milan Sonka[a]

The University of Iowa, [a]Department of Electrical and Computer Engineering and [b]Department of Biomedical Engineering Iowa City, IA 52242, USA

ABSTRACT

In vivo studies of the relationships that exist among vascular geometry, plaque morphology, and hemodynamics have recently been made possible through the development of a system that accurately reconstructs coronary arteries imaged by x-ray angiography and intravascular ultrasound (IVUS) in three dimensions. Currently, the bottleneck of the system is the segmentation of the IVUS images. It is well known that IVUS images contain numerous artifacts from various sources. Previous attempts to create automated IVUS segmentation systems have suffered from either a cost function that does not include enough information, or from a non-optimal segmentation algorithm. The approach presented in this paper seeks to strengthen both of those weaknesses — first by building a robust, knowledge-based cost function, and then by using a fully optimal, three-dimensional segmentation algorithm. The cost function contains three categories of information: a compendium of learned border patterns, information theoretic and statistical properties related to the imaging physics, and local image features. By combining these criteria in an optimal way, weaknesses associated with cost functions that only try to optimize a single criterion are minimized. This cost function is then used as the input to a fully optimal, three-dimensional, graph search-based segmentation algorithm. The resulting system has been validated against a set of manually traced IVUS image sets. Results did not show any bias, with a mean unsigned luminal border positioning error of 0.180 ± 0.027 mm and an adventitial border positioning error of 0.200 ± 0.069 mm.

Keywords: intravascular ultrasound, segmentation

1. INTRODUCTION

The mechanisms of plaque development in coronary arteries are not yet completely understood. A number of factors such as vascular geometry, plaque morphology, and coronary hemodynamics combine to influence the development of atherosclerotic plaques. Previously, we have developed a system that is capable of accurately reconstructing in vivo coronary arteries imaged with biplane angiography and intravascular ultrasound (IVUS).[1,2] Using this system, it has been possible to initiate studies on the relationships that exist among vascular geometry, plaque morphology, and hemodynamics.[3–7] These studies are now ready to be expanded to include a larger number of patients. In order to handle the larger number of patients that will be included in new studies, we present a method for highly automated segmentation of IVUS images.

Figure 1 shows a flow chart of our angio-IVUS fusion system. Despite years of research into automatic segmentation techniques, the processing of IVUS image data is still the major bottleneck of our fusion system and IVUS-driven clinical studies. Clearly, clinically acquired IVUS image data suffer from a limited image quality, mainly caused by the diseased nature of the imaged arteries. The IVUS image quality is adversely affected by presence of calcified plaques and by the presence of stents; however, they are more often present than not in the image data acquired from diseased subjects. Figure 2 demonstrates the lack of image information in a particular IVUS image frame. In the case of Figure 2, the lack of information is due to acoustic shadowing as a result of the density of the calcified plaque seen at four- to eight-o'clock in the image. Similar shadowing can also occur elsewhere in IVUS images as a result of implanted stents, guidewire artifacts, and vascular branchpoints. This lack of information can only be supplemented by three-dimensional (3-D) contextual information.

A number of IVUS image segmentation approaches have been explored by our research group, including dynamic programming with a fixed cost function, Active Appearance and Active Shape Models, and other

E-mail: <mark-olszewski@uiowa.edu>; Fax: +1-319-335-6028

Medical Imaging 2005: Image Processing, edited by J. Michael Fitzpatrick, Joseph M. Reinhardt, Proc. of SPIE Vol. 5747 (SPIE, Bellingham, WA, 2005)
1605-7422/05/$15 · doi: 10.1117/12.595850

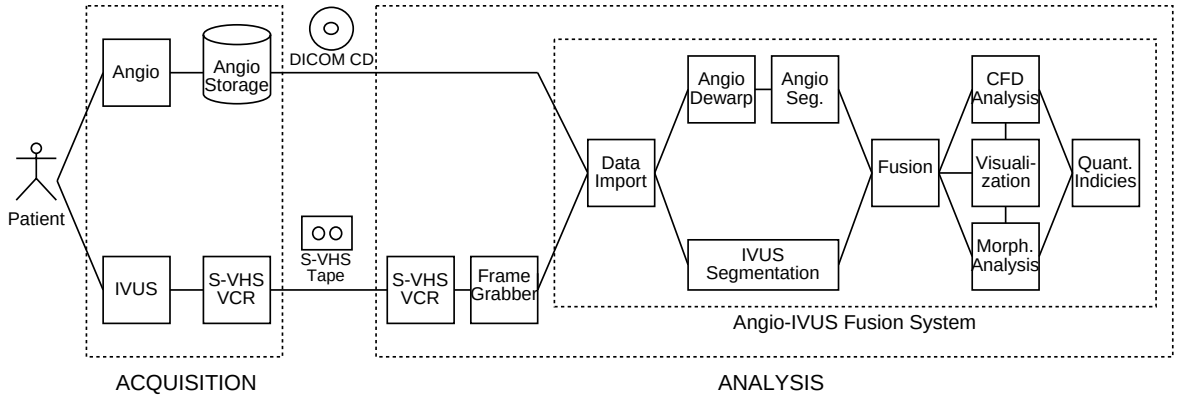

Figure 1. Angiography-intravascular ultrasound (IVUS) fusion system. Currently, the bottleneck of the processes leading to a geometrically correct three-dimensional reconstruction is the segmentation of the IVUS images.

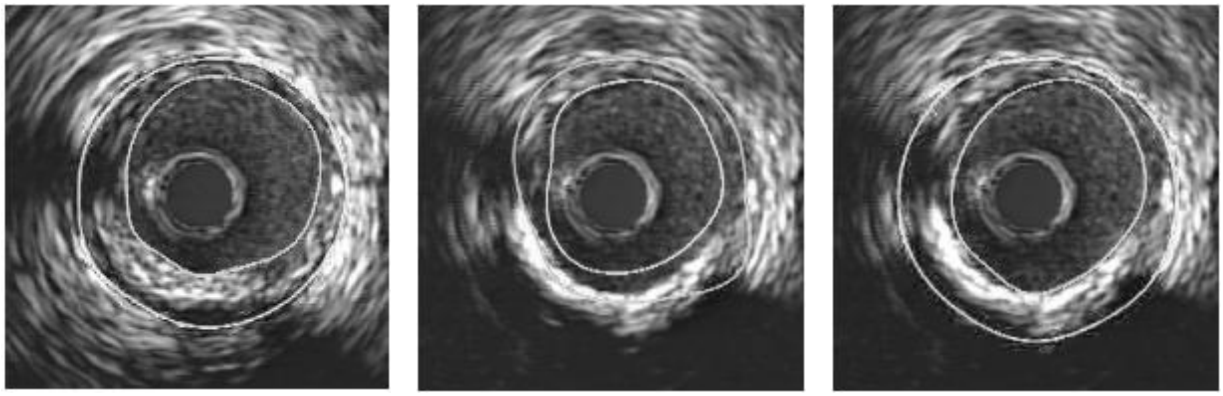

(a) (b) (c)

Figure 2. Role of 3-D context in IVUS segmentation. The goal of our segmentation routine is to be able to identify the luminal (inner) and media-adventitia (outer) borders in each frame. (a) Frame N: Media-adventitia border is well identified in this frame. (b) Frame N+1: Calcified plaque makes media-adventitia border segmentation unreliable if no 3-D context is used. The shadowing that hinders the detection of the border results from acoustic shadowing due to the density of the calcified plaque. (c) Contextual information present in adjacent frames allows reliable analysis of frame N+1.

model-based approaches. Our previous IVUS segmentation approach combined the use of dynamic programming with a cost function capable of learning its parameters from expert-traced examples. A scoring system was employed in combination with a multiresolution approach that mimics human vision.[8] While this automated IVUS segmentation system outperformed the previous approaches, it still did not perform sufficiently well to allow unsupervised analyses, most probably because it did not take sufficient advantage of higher dimensional spatiotemporal context; in other words, the fact that the individual borders are identified sequentially and not simultaneously adversely affected the method's performance.

2. METHODS

2.1. Preprocessing

Prior to segmenting the IVUS image data, several preprocessing steps occur. The IVUS pullback is automatically centered, the field of view is identified, and the region containing the catheter is excluded from further analysis using an implementation of the Hough Transform. Also, stationary image components that may contain a gain offset or stationary artifacts such as the catheter ring-down are removed by subtracting the average pullback frame from each image in the pullback. The removal of stationary components serves as a normalization step for the learning process described in the next section, and removes any biases that may corrupt the statistical analyses also described below. The final step before beginning processing is to "unfold" the IVUS pullback so that the cylindrical surface detection problem is reformatted into an elevation map detection problem. This process is shown in Figure 3.

2.2. Optimal Three Dimensional Graph Search

A method for efficient detection of the *globally optimal* surfaces representing object boundaries in volumetric datasets was recently developed by our research group,[9,10] and is the cornerstone of this IVUS segmentation system. The method is capable of simultaneously detecting multiple interacting surfaces, in which the optimality is not only controlled by the cost functions designed for individual surfaces, but also confined by several geometric constraints defining the surface smoothness and interrelations. The method solves the surface detection problems by transforming the detection problem into computing minimum s-t cuts in the derived geometric hypergraphs. The proposed algorithm has polynomial complexity, is computationally efficient, and allows simultaneous segmentation of the lumen-plaque and media-adventitia interface surfaces in the 3-D IVUS pullback data. Consequently, the spatial and temporal contextual information is incorporated in a single optimization process yielding a pair of interacting surfaces in 3-D.

To further improve the efficiency of the algorithm and its robustness to noise and artifact, the automated system uses the optimal surface detection technique in a multiresolution approach. This is achieved by finding the optimal luminal and medial-adventitial borders in a three-tiered sequence starting at a low resolution and continuing to a high resolution. At each resolution stage, the searched area of the graph is reduced so that more efficient use of computation time is made.

2.3. Cost Function Design

The cost functions used for the identification of the luminal and adventitial surfaces of the IVUS data are of paramount importance for the success of the segmentation. Experience has led to the conclusion that a successful cost function will contain three classes of information at both a global and a local level: expected border properties, information theoretic criteria based on the statistical properties of ultrasound, and regional homogeneity properties. By combining these three types of information in an optimal manner, the overall segmentation process is able to overcome the variation and artifacts that are so often a part of IVUS imaging. These classes are realized as a combination of the following terms:

1. Intensity patterns learned from example;
2. Rayleigh distribution models of ultrasound image data[11–13];
3. Object homogeneity properties.[14]

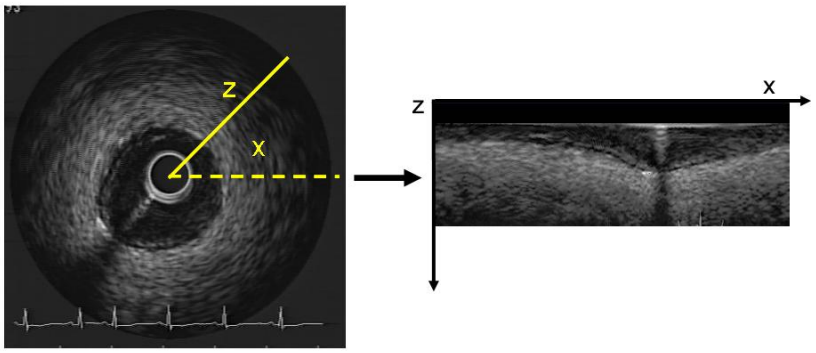

(a) Polar coordinate transform of an IVUS frame.

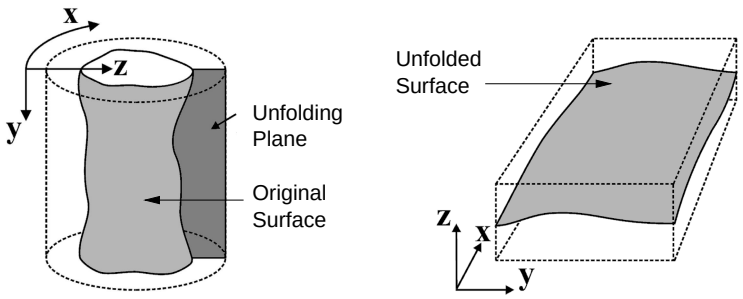

(b) Polar coordinate transform of a cylindrical surface.

Figure 3. Polar coordinate transform. (a) "Unfolding" an IVUS image frame using a polar transform. (b) This process is applied to the IVUS pullback, so that the detection of the cylindrical surfaces of varying radius is transformed to the detection of an elevation map of varying height.

Multiresolution methods[15] and methods that attempt to integrate edge and region information[16] have proven to be successful in the past. The combination of local and global features of this cost function will seek to minimize the drawbacks associated with previous techniques that concentrated on only one level, while the combination of analytical and learned terms will allow the system to learn the properties of features that are not easily expressed analytically, while retaining analytical terms to help when a particular feature has not yet been seen by the system.

2.3.1. Learned border patterns

It has been observed that although noise, speckle, and artifacts tended to confuse previous automated methods, human tracers are still able to correctly segment the vast majority of IVUS images. This observation motivated the design of a cost function that consisted of terms that were learned from experience, in addition to those that were derived analytically from the data being analyzed.

Over time, there has been an accumulation of both manually traced IVUS data sets and IVUS data sets that have been semi-automatically segmented with manual correction. These data sets were used in the development of a cost function to learn what pixels the human observer most often chooses for border pixels. In order to perform the learning step, a window is passed over the training images. Within the window, the pattern of pixels is examined. For each pattern that contains a border pixel, the system increments an accumulator entry corresponding to that border pattern, as shown in Figure 4(a) for a 2-D case. An accumulator entry exists for every possible pattern, following normalization and quantization to allow for image variation and memory

conservation, respectively. The accumulator can now be considered to contain the likelihood of each pattern being a border pattern.

After this training stage is complete, the learned information can be used to score an image that is to be analyzed. In the same way that the accumulator was created in the training step, patterns are examined in the image. Then, a cost image is generated by assigning a likelihood value to the pixel based on the value found in the accumulator for the same pattern, as shown in Figure 4(b) for a 2-D case. This process results in costs for both the luminal and medial-adventitial borders. The learned border properties may also be updated continually as the system is in use, thereby permitting the system to gain knowledge over time and get better with age.

2.3.2. Statistical properties of ultrasound

It has been known for some time that the developed speckle in ultrasonic images is characterized by a Rayleigh distribution, given by:[11, 12]

$$P(A_i) = \frac{A_i}{\alpha^2} \exp(-\frac{A_i^2}{2\alpha^2}) \tag{1}$$

where $P(A_i)$ represents the probability that pixel i has intensity A_i.

Recently, this knowledge has been used in the accurate segmentation of the luminal boundary in IVUS images by deformable contours that separate two regions (lumen and vessel wall) based on their global statistical properties.[13] To adapt this concept to our optimal 3D graph approach, the objective function for the contour estimation was approximated to produce a voxel cost at the polar-transformed image location $I(x, y, z)$ (Figure 3(b)) that is expressed as:

$$C_{Rayleigh}(x, y, z) = -z \ln(\hat{\alpha}_1^2) - (Z - z) \ln(\hat{\alpha}_2^2) \tag{2}$$

where Z is the height of the polar-transformed image and $\hat{\alpha}_1$ and $\hat{\alpha}_2$ are approximated as:

$$\hat{\alpha}_1 = \sqrt{\frac{1}{2z} \sum_{z'=0}^{z' \le z} I(x, y, z')^2} \tag{3}$$

$$\hat{\alpha}_2 = \sqrt{\frac{1}{2(Z - z)} \sum_{z'=z+1}^{z' < Z} I(x, y, z')^2} \tag{4}$$

2.3.3. Region homogeneity

Degradations in image quality due to severe vascular disease or videotape recording artifact can alter the development of a true Rayleigh distribution in the image speckle. Therefore, we chose to add a version of the Chan-Vese minimum variance criterion[14] as a third component of our cost function. This term allows allows segmentation without the presence of gradients, and without the assumption of a particular statistical model. As with the Rayleigh cost term, the Chan-Vese functional is restated so that it produces a voxel cost as:

$$C_{CV}(x, y, z) = \sum_{z'=0}^{z' \le z} (I(x, y, z') - a_1)^2 + \sum_{z'=z+1}^{z' < Z} (I(x, y, z') - a_2)^2 \tag{5}$$

where a_1 and a_2 are approximated as:

$$\hat{a}_1 = mean(I(\mathbf{x}, \mathbf{y}, \mathbf{z}_1)) \tag{6}$$

$$\hat{a}_2 = mean(I(\mathbf{x}, \mathbf{y}, \mathbf{z}_2)) \tag{7}$$

$I(\mathbf{x}, \mathbf{y}, \mathbf{z}_1)$ and $I(\mathbf{x}, \mathbf{y}, \mathbf{z}_2)$ correspond to nodes below and above the surface, respectively.

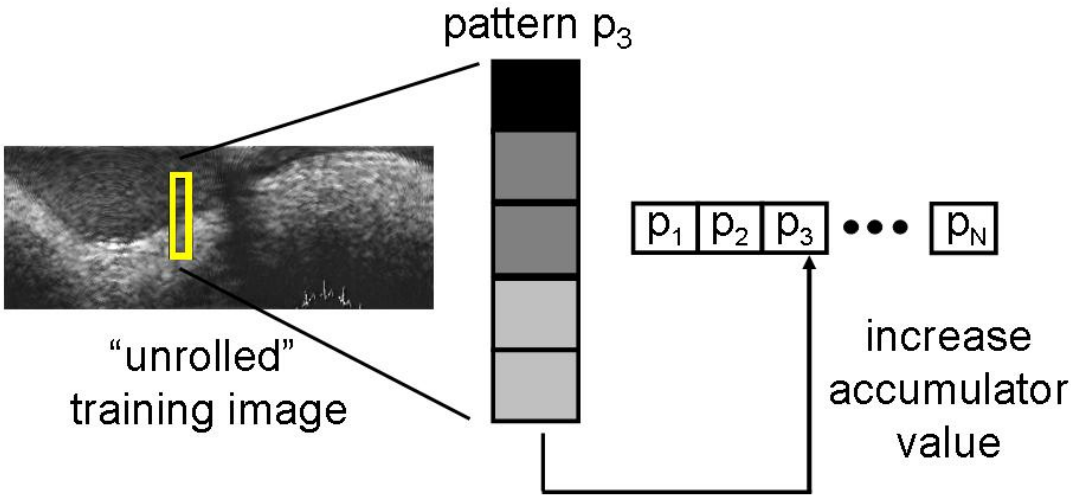

(a) Learning the patterns associated with border pixels.

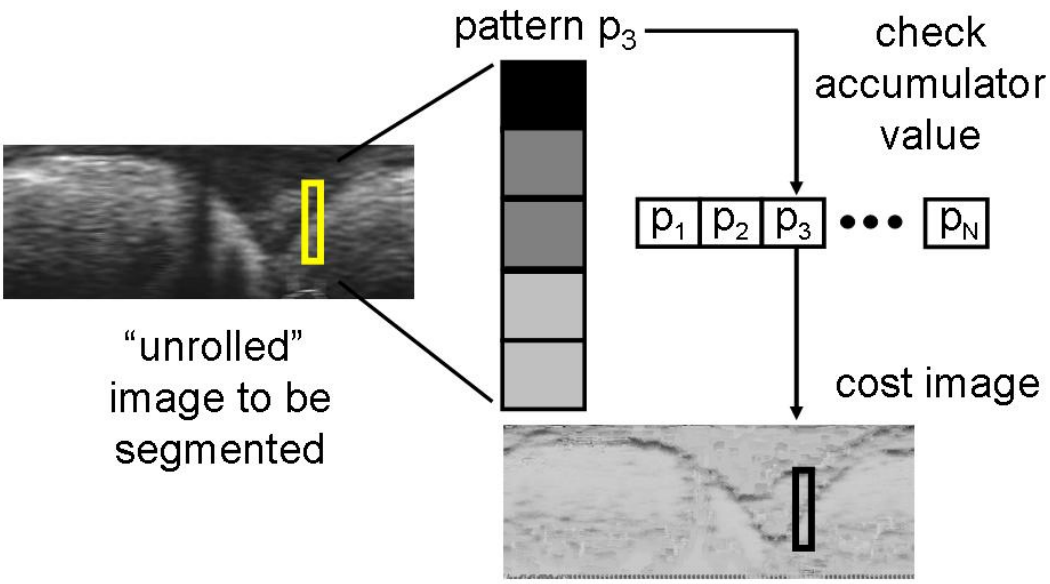

(b) Using the accumulated knowledge to build a cost function.

Figure 4. Learned border patterns. A set of training images that have been segmented manually are examined. An accumulator is created that represents a range of patterns. The accumulator entries corresponding to border patterns are increased with every incidence of that border pattern in the training set. Later, when a new image is analyzed, the accumulator values are used to assign the likelihood of each pattern in the new image being a border pattern. The result is a cost image that contains the likelihood of each pixel being a border pixel. In the figure, this cost image has been inverted to fit graph-based segmentation techniques that try to minimize cost.

	Lumen	Adventitia
Signed Mean ± SD (mm)	0.042 ± 0.062	-0.007 ± 0.108
Unsigned Mean ± SD (mm)	0.180 ± 0.027	0.200 ± 0.069
Maximum (mm)	0.236	0.300

Table 1. Segmentation border positioning errors for corresponding points on the luminal and medial-adventitial surfaces in 21 vessels.

2.3.4. Combination of cost terms

The developed cost terms are combined into a total cost function in a pseudoprobabilistic manner such that the final segmentation produces a result that is optimal with regards to all of the terms. Prior to combination, the terms are each normalized so that they fall in the range $0 \leq C_n \leq 1$, where C_n represents any cost term. In this manner, each term can be thought of as the likelihood that a certain voxel exhibits the feature that the term represents. Then, the term that jointly estimates the combination of cost terms can be represented as the product of the individual normalized terms. The learned terms and the Rayleigh separation term must be inverted in order to search for the minimum cost path, since they are maximal at the probable border locations. Also, since an additive procedure is used in the optimization, the logarithm of the product is taken at each voxel so that when the optimal surfaces are detected, it ensures that each surface optimally maximizes the joint likelihood of the cost terms over each border. The Rayleigh separation term is omitted from the cost of the adventitial surface because it is only well defined for a single separation point. The total cost for each border is then expressed as:

$$C_{totalLumen}(x,y,z) = \log((1 - \|C_{learnedLumen}(x,y,z)\|) \bullet (1 - \|C_{Rayleigh}(x,y,z)\|) \bullet \|C_{CV}(x,y,z)\|) \quad (8)$$

$$C_{totalAdventitia}(x,y,z) = \log((1 - \|C_{learnedAdventitia}(x,y,z)\|) \bullet \|C_{CV}(x,y,z)\|) \quad (9)$$

3. RESULTS

The segmentation system was tested on a set of 21 in-vivo IVUS pullbacks containing a mixture of each of the three major coronary arteries (5 left circumflex arteries, 8 left anterior descending arteries, 8 right coronary arteries, 3288 total frames). The vessels were imaged during routine cardiac catheterization and were generally quite diseased. Image aquisition was performed using a Boston Scientific 40 MHz IVUS catheter connected to a Boston Scientific Clearview IVUS console. Each pullback was recorded on S-VHS tape and digitized to an image size of 384 x 384 pixels. The image field of view covered 8-10 mm, and the pullback speed was 0.5 mm/s.

Following the optimal three dimensional segmentation, luminal and medial-adventitial borders were available for each vessel. These borders were compared with independent, expertly identified borders that had been manually traced. In each instance, the vessel being segmented was left out of the training set used for the cost function design. Regions containing stents, branchpoints with diameter greater than 0.5 mm, and regions containing calcifications with greater than 30 degrees of occlusive shadowing were excluded from analysis. These regions leave little room for anything except subjective assessment by the expert tracer, and are excluded from further analysis due to the uncertainty of the clinical usefulness of parameters derived from segmentation of these regions.

The differences between the detected borders and the manually traced borders were computed for 720 corresponding points (every half degree angularly) on each border and are given in Table 1. As shown in the table, the signed mean errors for both surfaces are near zero. Thus, it is shown that the algorithm is unbiased (neither consistently underestimating, nor consistently overestimating) the border positions. The unsigned mean error is in good agreement with the expert observer, although more detailed analysis of inter- and intra-observer variability in similar data are needed before the results can really be put into context. Figure 5 shows an example of a segmented data set. It is worth noting the system achieved these results without any user interaction.

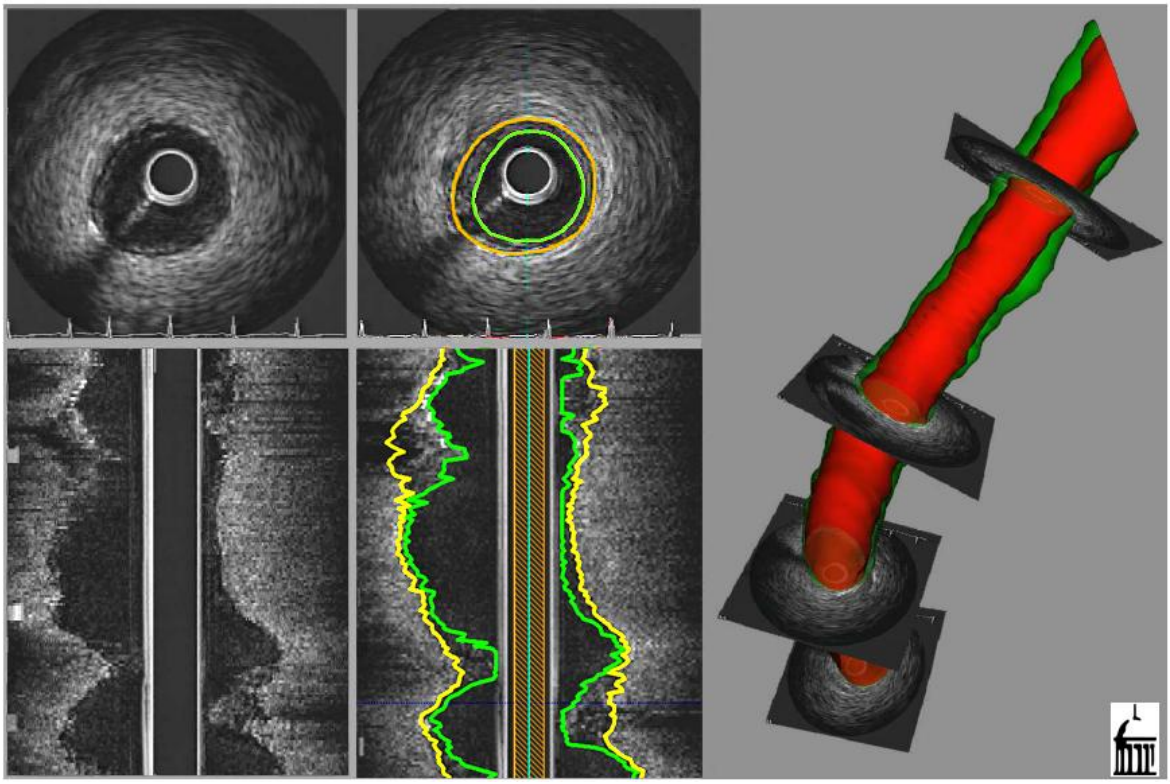

Figure 5. Lumen-intima and media-adventitia interface segmentation in an IVUS image sequence. On the left, the original cross-sectional and long-axis data are shown. In the middle, the segmentation result shows the luminal and medial-adventital borders. On the right, a 3-D reconstruction shows the luminal and medial-adventitial interfaces as they pass through the IVUS data.

4. CONCLUSIONS

In conclusion, a system for the automated segmentation of IVUS images has been presented. The results obtained agree with manually traced contours for the same vessels while dramatically decreasing the processing time for generating accurate 3-D reconstructions of coronary arteries. The accurate segmentation, combined with the substantial improvement in processing time, will allow a larger clinical study investigating the relationships between plaque development, vascular geometry, and coronary hemodynamics; the system will also aid other IVUS-based studies that must handle large quantities of data.

5. ACKNOWLEDGMENTS

This work was supported in part by grant R01 HL63373 of the National Heart Lung and Blood Institute at the National Institutes of Health, Bethesda MD. Kang Li and Xiaodong Wu, of the University of Iowa Department of Electrical and Computer Engineering, and Danny Chen, of the University of Notre Dame, deserve great thanks for their development of the optimal surface detection theory and library. The authors would like to thank James D. Rossen, Theresa M. H. Brennan, and Kathleen C. Braddy, of the University of Iowa Department of Internal Medicine, and John J. Lopez, of the University of Chicago, for performing the cardiac catheterization procedures. Also, the authors would like to thank Rubén Medina, Universidad de Los Andes, Facultad de Ingeniería, Mérida (Venezuela); Peter H. Stone and Charles L. Feldman, both of Brigham & Women's Hospital, Cardiovascular Division, Boston MA; and A. Ümit Coşkun, Northeastern University, Mechanical / Industrial / Manufacturing Engineering, Boston MA, for their contributions and feedback during the development of this system.

REFERENCES

1. A. Wahle, G. P. M. Prause, S. C. DeJong, and M. Sonka, "Geometrically correct 3-D reconstruction of intravascular ultrasound images by fusion with biplane angiography — methods and validation," *IEEE Transactions on Medical Imaging* **18**, pp. 686–699, Aug. 1999.
2. M. E. Olszewski, A. Wahle, R. Medina, S. C. Mitchell, and M. Sonka, "Integrated system for quantitative analysis of coronary plaque via data fusion of biplane angiography and intravascular ultrasound," in *Computer Assisted Radiology and Surgery (CARS 2003)*, H. U. Lemke, K. Inamura, M. W. Vannier, A. G. Farman, K. Doi, and J. H. C. Reiber, eds., *Excerpta Medica International Congress Series* **1256**, pp. 1117–1122, Elsevier, (Amsterdam), 2003.
3. A. Wahle, R. Medina, K. C. Braddy, J. M. Fox, T. M. H. Brennan, J. J. Lopez, J. D. Rossen, and M. Sonka, "Impact of local vessel curvature on the circumferential plaque distribution in coronary arteries," in *Medical Imaging 2003: Physiology and Function: Methods, Systems, and Applications*, A. V. Clough and A. A. Amini, eds., **5031**, pp. 204–213, SPIE Proceedings, (Bellingham WA), 2003.
4. A. Wahle, S. C. Mitchell, S. D. Ramaswamy, K. B. Chandran, and M. Sonka, "Four-dimensional coronary morphology and computational hemodynamics," in *Medical Imaging 2001: Image Processing*, M. Sonka and K. M. Hanson, eds., **4322**, pp. 743–754, SPIE Proceedings, (Bellingham WA), 2001.
5. R. Medina, A. Wahle, M. E. Olszewski, and M. Sonka, "Three methods for accurate quantification of plaque volume in coronary arteries," *International Journal of Cardiovascular Imaging* **19**, pp. 301–311, Aug. 2003.
6. A. Wahle, M. E. Olszewski, and M. Sonka, "Interactive virtual endoscopy in coronary arteries based on multi-modality fusion," *IEEE Transactions on Medical Imaging — Virtual Endoscopy* **23**, pp. 1391–1403, November 2004.
7. A. Wahle, J. J. Lopez, M. E. Olszewski, S. C. Vigmostad, K. C. Braddy, T. M. H. Brennan, S. W. Bokhari, J. G. Bennett, E. M. Holper, J. D. Rossen, K. B. Chandran, and M. Sonka, "Relationship between plaque development and local hemodynamics in coronary arteries," in *Medical Imaging 2005: Physiology, Function, and Structure from Medical Images*, A. A. Amini and A. Manduca, eds., **5746**, SPIE Proceedings, (Bellingham WA), 2005.
8. M. E. Olszewski, A. Wahle, S. C. Mitchell, and M. Sonka, "Segmentation of intravascular ultrasound images: A machine learning approach mimicking human vision," in *Computer Assisted Radiology and Surgery (CARS 2004)*, pp. 1045–1049, (Amsterdam), 2004.
9. K. Li, D. Chen, and M. Sonka, "Efficient optimal surface detection: Theory, implementation and experimental validation," in *Medical Imaging 2004: Image Processing*, M. Sonka and J. M. Fitzpatrick, eds., **5370**, pp. 620–627, SPIE Proceedings, (Bellingham WA), 2004.
10. K. Li, X. Wu, D. Z. Chen, and M. Sonka, "Globally optimal segmentation of interacting surfaces with geometric constraints," in *Proceedings, IEEE Computer Society Conference on Computer Vision and Pattern Recognition (CVPR)*, pp. 394–399, (Piscataway, NJ), June 2004.
11. C. B. Burckhardt, "Speckle in ultrasound B-mode scans," *IEEE Transactions on Sonics and Ultrasonics* **SU-25**, pp. 1–6, January 1978.
12. R. F. Wagner, S. W. Smith, J. M. Sandrik, and H. Lopez, "Statistics of speckle in ultrasound B-scans," *IEEE Transactions on Sonics and Ultrasonics* **30**, pp. 156–163, May 1983.
13. E. Brusseau, C. L. de Korte, F. Mastik, J. Schaar, and A. F. W. van der Steen, "Fully automatic luminal contour segmentation in intracoronary ultrasound imaging — a statistical approach," *IEEE Transactions on Medical Imaging* **23**, pp. 554–566, May 2004.
14. T. F. Chan and L. A. Vese, "Active contours without edges," *IEEE Transactions on Image Processing* **10**, pp. 266–277, February 2001.
15. Q. Liang, I. Wendelhag, J. Wikstrand, and T. Gustavsson, "A multiscale dynamic programming procedure for boundary detection in ultrasonic artery images," *IEEE Transactions on Medical Imaging* **19**, pp. 127–142, February 2000.
16. A. Chakraborty, L. H. Staib, and J. S. Duncan, "Deformable boundary finding in medical images by integrating gradient and region information," *IEEE Transactions on Medical Imaging* **15**, pp. 859–870, December 1996.